Article

Block copolymer-assisted solvothermal synthesis of hollow BiMoO spheres substituted with samarium

Raana Kashfi Sadabad, Sajad Yazdani, Abdolali Alemi, Tran Doan Huan, Rampi Ramprasad, and Michael Thompson Pettes

Langmuir, **Just Accepted Manuscript** • DOI: 10.1021/acs.langmuir.6b02854 • Publication Date (Web): 30 Sep 2016

Block copolymer-assisted solvothermal synthesis of hollow Bi_2MoO_6 spheres substituted with samarium

Raana Kashfi-Sadabad,[a,b] Sajad Yazdani,[c] Abdolali Alemi,[b] Tran Doan Huan,[d] Rampi Ramprasad,[a,d] and Michael Thompson Pettes[a,c*]*

[a] *Institute of Materials Science, University of Connecticut, Storrs, Connecticut 06269, USA*
[b] *Inorganic Chemistry Department, University of Tabriz, C.P. 51664 Tabriz, Iran*
[c] *Department of Mechanical Engineering, University of Connecticut, Storrs, Connecticut 06269, USA*
[d] *Materials Science & Engineering Department, University of Connecticut, Storrs, Connecticut 06269, USA*

**Authors to whom correspondence should be addressed. Email: ra.kashfi@gmail.com, michael.pettes@uconn.edu*

Table of Contents/Abstract Graphic.

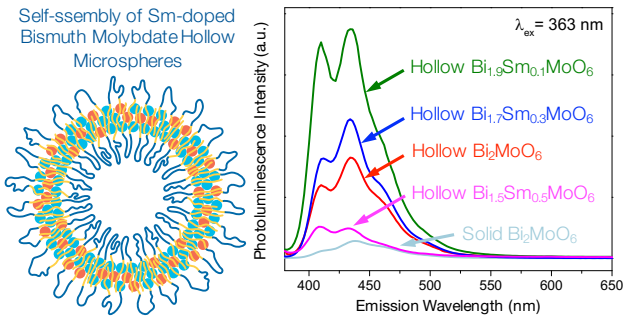

Abstract

Hollow spherical structures of ternary bismuth molybdenum oxide doped with samarium ($Bi_{2-x}Sm_xMoO_6$) were successfully synthesized via development of a Pluronic P123 (PEO_{20}-PPO_{70}-PEO_{20})-assisted solvothermal technique. Density functional theory (DFT) calculations have been performed to further understand the effects of Sm doping on the electronic band structure, density of states, and band gap of the material. The calculations for $0 \leq x \leq 0.3$ revealed a considerably flattened conduction band minimum near the Γ point suggesting that the material can be considered to possess a quasi-direct band gap. In contrast, for $x = 0.5$ the conduction band minimum is deflected towards the U point making it a distinctly indirect band gap material. The effects of a hollow structure as well as Sm substitution on the absorbance and fluorescence

properties of the materials exhibited increased emission intensities at low Sm concentrations (x = 0.1 and 0.3) with x = 0.1 displaying a peak photoluminescence intensity 13.2 times higher than for the undoped bulk sample. Subsequent increases in the Sm concentration resulted in quenching of the emission intensity, indicative of the onset of a quasi direct-to-indirect electronic band transition. These results indicate that both mesoscale structuring and Sm doping will be promising routes to tune optoelectronic properties for future applications such as catalysis and photocatalysis.

Introduction

Hollow-structuring is an effective materials engineering approach that can tailor properties for many different energy-related applications by increasing the surface-to-volume ratio and reducing charge and mass diffusion lengths.[1-3] One reason that hollow structures are interesting for the preparation of complex oxides is that the enhanced surface area can provide more oxygen vacancies and defects which may benefit the optical properties of the materials.[4] Hollow-spherical structures have been prepared using various synthetic techniques.[2, 5] In particular, hard and soft templating methods have been demonstrated as effective approaches to successfully synthesize these hollow structures.[6] The latter technique (soft templation) is known to have several advantages over the other methods, such as producing porous shell structures which are attractive candidates for encapsulation among other applications. This allows retention of the mesoscale morphology upon removal of the surfactant, as opposed to the hard templation method where degradation may occur during or after the template etching process.[7]

Bismuth molybdate is a layered perovskite and one of the members of Aurivillius oxide family which have perovskite-like and fluorite-like blocks.[8] Interesting catalytic, dielectric and luminescence properties make these materials attractive for further studies, especially on their fundamental physical and chemical behaviors.[9-13] Several studies have been conducted to control the shape and the structure of Bi_2MoO_6 for various applications.[10, 14-16] In regard to hollow structuring, cage-like Bi_2MoO_6 hollow spheres have been synthesized using a hard template of colloidal carbon spheres[17] and a synthesis of hierarchical flower-like Bi_2MoO_6 hollow spheres was reported using a template-free solvothermal approach.[15] Due to the thermal and chemical stability as well as the comparable ionic radius of Bi^{3+} with those of the lanthanide ions, Bi_2MoO_6 can be considered as a proper host for rare-earth dopants. Understanding the physical and chemical processes of such lanthanide ion-doped Bi_2MoO_6 materials is fruitful as the appropriate design can

reduce the need for pure (and scarce) rare earth-based materials.[18] In a previous studies, photocatalytic properties of Bi_2MoO_6 doped with Gd^{3+}, Ho^{3+} and Yb^{3+} ions[19] and Eu^{3+} ions[20], and their corresponding luminescence properties have been reported.

In the current study, we present the modulation in optical properties of $Bi_{2-x}Sm_xMoO_6$ due to both hollow structuring and alloying with samarium. We have developed a self-assembly technique to synthesize uniform hollow spheres of Bi_2MoO_6 and $Bi_{2-x}Sm_xMoO_6$ (x = 0.1, 0.3 and 0.5) using Pluronic P123 ($EO_{20}PO_{70}EO_{20}$) as a soft templating agent. The copolymer, inorganic precursors, and solvent interactions were found to favor formation of vesicles resulting in hollow structures that are obtained at specific thermal conditions and polymer concentrations through chemical self-transformation. The results of this study show a pathway for the synthesis of Bi_2MoO_6-based materials with hollow structures and successful incorporation of lanthanide elements (here Sm), and reveal the importance of certain synthesis conditions that need to be controlled in order to obtain the desired mesostructure. In addition, density functional theory (DFT) calculations were performed to identify the fundamental mechanisms responsible for the behavior of the material in response to Sm substitution, especially changes in the electronic band structure.

Experimental Section

Chemicals. Bismuth(III) nitrate pentahydrate [$Bi(NO_3)_3{\cdot}5H_2O$, ≥98.0%], phosphomolybdic acid hydrate $H_3[P(Mo_3O_{10})_4]{\cdot}xH_2O$, 1-butanol (anhydrous, 99.8%) and poly(ethylene glycol)-block-poly(propylene glycol)-block-poly(ethylene glycol) PEO_{20}–PPO_{70}–PEO_{20} (Pluronic P123) were obtained from Sigma-Aldrich. Concentrated nitric acid (HNO_3, 68–70%) was obtained from J. T. Baker. All chemicals were used as received and used without further purification.

Synthesis of sphere-like hollow Bi_2MoO_6 microspheres. For preparation of the undoped samples, 1 g of nitric acid (HNO_3) was added to 20 g 1-butanol at 75 °C and was stirred for 5 min, after which 8 mmol of bismuth(III) nitrate pentahydrate (3.88 g) was dissolved in the above solution. Then a stoichiometric amount of phosphomolybdic acid hydrate as the Mo source (0.608 g) was slowly added to the mixture to form a transparent yellowish solution. Subsequently, between 1 and 3 g of P123 was added. After vigorous stirring for ~15 min, the suspension was sealed in a Teflon-lined stainless steel autoclave. The autoclave was kept at 160 °C for 3 h and

then was cooled naturally to room temperature. The precipitate was obtained by centrifugation and sequential washing with ethanol several times, then drying at 80 °C for 6 h. In order to remove the soft template, the obtained materials were calcined under air at 450 °C for 4 h with a heating/cooling ramp rate of 2 °C/min. For comparison with the hollow Bi_2MoO_6 spheres, solid Bi_2MoO_6 powder was prepared as described above but without the addition P123.

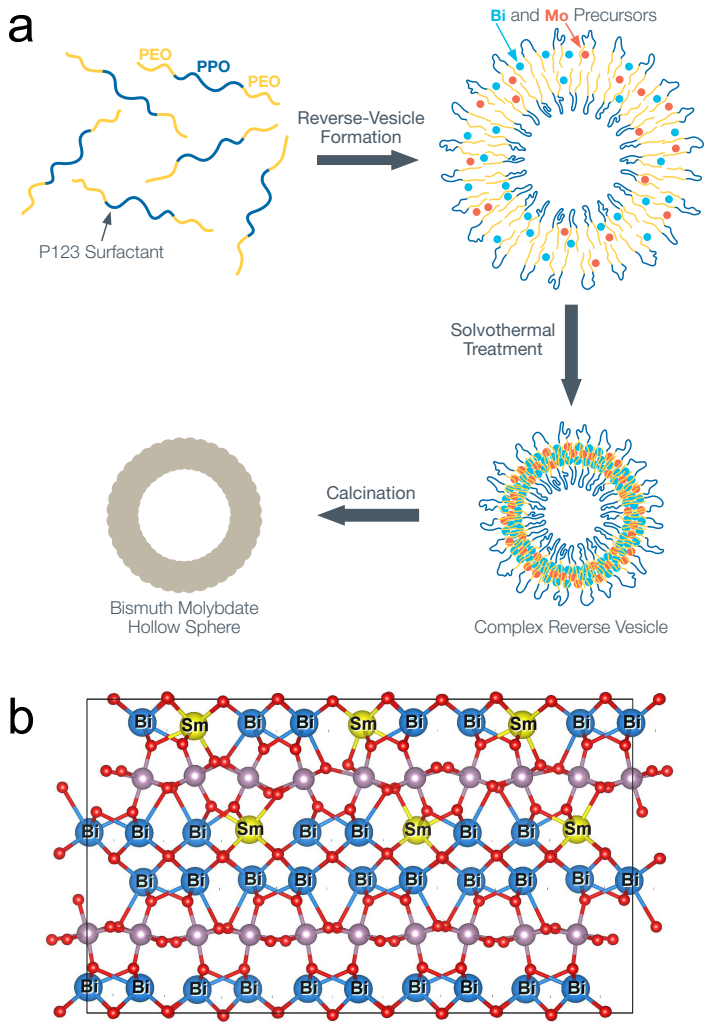

Scheme 1. *(a) The formation of hollow shell structures by P123 soft templated solvothermal method. (b) Unit cell crystal structure of orthorhombic Sm-doped* Bi_2MoO_6 *using the VESTA program. Bismuth and samarium atoms are labeled by names while molybdenum and oxygen atoms are indicated by colors (gray and red, respectively).*

Synthesis of hollow $Bi_{2-x}Sm_xMoO_6$ microspheres. $Bi_{2-x}Sm_xMoO_6$ (x = 0.1, 0.3 and 0.5) was prepared by a similar procedure, except that additional dopant ions were added to the solution before the addition of P123. For instance, to synthesize the $Bi_{1.9}Sm_{0.1}MoO_6$, 0.05 mmol of Sm_2O_3

was added to a solution of 20 g 1-butanol containing previously described amounts of bismuth (III) nitrate and phosphomolybdic acid hydrate. The formation mechanism and crystal structure are depicted in Scheme 1.

Characterization. Powder X-ray diffraction analyses (XRD) were conducted on a Rigaku Ultima IV diffractometer with Cu Kα radiation (λ = 1.5406 Å) at room temperature. Brunauer−Emmett−Teller (BET) specific surface areas and Barrett-Joyner-Halenda (BJH) pore size distributions were calculated using nitrogen sorption isotherms measured on a Micrometrics ASAP 2010 instrument. Before each measurement, samples were degassed at 120 °C for 7 h in order to remove the adsorbed species. A Hi-Res TA 2950 thermogravimetric analyzer with 60 mL/min of air flow was used to perform thermogravimetric analyses (TGA) from 25 to 800 °C at a heating rate of 10 °C/min. X-ray photoelectron spectroscopy (XPS) was conducted on a ΦPhysical Electronics Industries model 590 spectrometer with multipoles, using Al Kα radiation (1486.6 eV). A JEOL 2010 FasTEM and a FEI Talos F200X TEM/STEM at an accelerating voltage of 200 kV were employed to perform phase contrast and scanning transmission electron microscopy (S/TEM) analysis. Field emission scanning electron microscopy (SEM, FEI Nova Nano SEM 450) was performed at an accelerating voltage of 2.0 kV. Diffuse-reflectance spectra were collected using a Shimadzu UV-2450 UV-Vis spectrophotometer; for each measurement, 0.2 g of solid sample was diluted in 2 g of $BaSO_4$. Raman spectroscopy was carried out using a Renishaw 2000 Raman microscope at 514 nm. Fourier transform-infrared spectra (FT-IR) were collected with a Nicolet Magna 560 spectrometer using a TGS detector. A Perkin Elmer Optima 7300DV was used in order to perform inductively coupled plasma optical emission spectroscopy (ICP/OES), where approximately 0.2 g of the sample was removed, homogenized, and placed into a hot block tube. Trace metal grade hydrochloric (3.6 mL) and nitric (1.2 mL) acids were added to each tube and placed in the hot block and refluxed for 3 h at 95 ºC. The samples were then cooled and brought up the final volume of 25 ml with deionized water after which ICP/OES analysis was performed. A Horiba Jobin Yvon SPEX Fluorolog 3-211 spectrofluorometer with a photomultiplier tube near-IR detector was used to measure the spectra of composite KBr/$Bi_{2-x}Sm_xMoO_6$ pellets. Photoluminescence (PL) spectroscopy measurements were performed using a Fluorolog 3-211, where an increment of 2 nm was used to collect both excitation and emission spectra.

First-principles calculations. The computational method used in this study is density functional theory (DFT) as implemented in the Vienna Ab Initio Simulation Package (VASP).[21, 22] The total energies of the examined structural models, E_{DFT}, were calculated with the Perdew-Burke-Ernzerhof (PBE) exchange-correlation (XC) functional[23] while the Brillouin zones of the models were sampled by a Monkhorst-Pack *k*-point mesh[24] of 1 × 1 × 5. The basis set used for our calculations includes all the plane waves of kinetic energy up to 400 eV. Convergence was assumed when the residual forces were smaller than 10^{-2} eVÅ^{-1}. For Bi, Mo, Sm, and O, the valence electrons were taken to be $5d^{10}6s^26p^3$, $4s^25s^24p^64d^5$, $5s^26s^25p^65d^1$, and $2s^22p^4$ respectively. Within these formalisms, the calculated band gap of pure Bi_2MoO_6 is E_g = 2.25 eV, which is about 20–30 % smaller than the experimental value of ~2.74 eV. This systematic reduction is well-known within the framework of DFT with semi-local XC functionals like PBE. Other than this, the dispersion of the calculated band structures is expected to be qualitatively accurate while errors in the lattice parameters from our calculations are within 1–2 %.

Results and Discussion

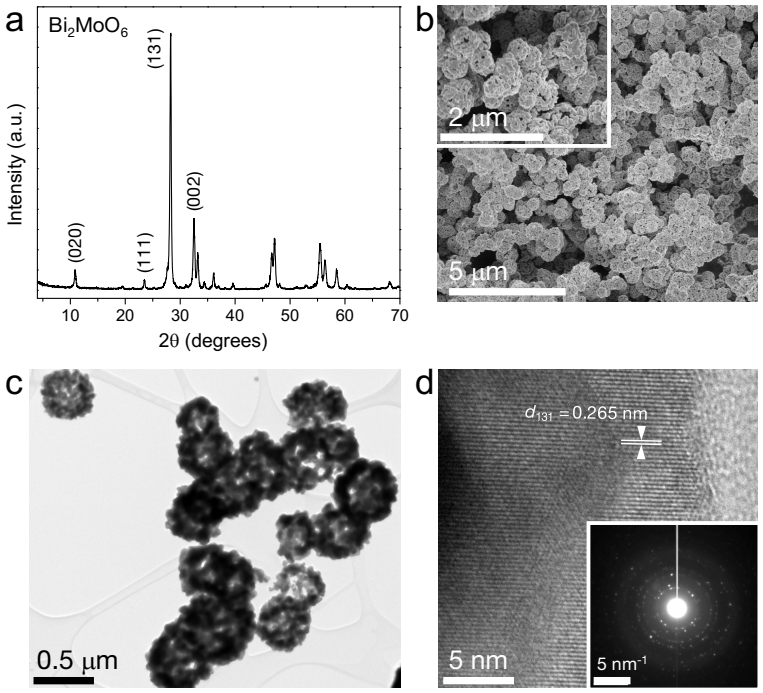

Figure 1. *(a) XRD pattern, (b) SEM images, (c) low- and (d) high- resolution TEM images of homogeneous, hollow Bi_2MoO_6 spheres.*

The composition and phase purity of the as-obtained products were characterized by powder XRD. Figure 1a displays the XRD patterns of hollow sphere Bi_2MoO_6 obtained by the solvothermal method after removing the P123 surfactant. All of the Bragg diffraction peaks in the range of $2\theta = 4–70°$ can be indexed to the pure orthorhombic phase of Bi_2MoO_6 (JCPDS file card no. 21-0102). The strong and sharp diffraction peaks in the pattern indicated that the as-obtained product was well crystallized.

According to thermogravimetric analysis (TGA) of Bi_2MoO_6 before calcination, weight losses of ~ 4.64, 11.32 and 3.68 % were observed in the temperature ranges of 25–150, 150–336, and 336–470 °C respectively (Figure S1a, Supporting Information). The three weight losses can be attributed to the removal of adsorbed water or butanol, decomposition of $Bi(NO_3)_3$, and oxidation of P123, respectively. These trends can be better understood when compared to the decomposition ranges of pristine $Bi(NO_3)_3 \cdot 5H_2O$ (mainly 120–200 °C and partially 200–600 °C), $H_3[P(Mo_3O_{10})_4] \cdot xH_2O$ (30–150 °C) and P123 (180–350 °C) as shown in Figure S1b–d of the Supporting Information. In addition, FT-IR results further confirmed that P123 was fully removed after calcination at 450 °C (Figure S1e, Supporting Information).

The structures of the Bi_2MoO_6 samples were investigated by SEM and TEM (shown in Figure 1b,c), where hollow Bi_2MoO_6 spheres were observed to have a relatively narrow size distribution of ~300–450 nm. In the TEM images, contrast between the dark edge and the brighter center was due to the large void in center of the hollow spheres. The shell thickness was observed to be in the range of 60–80 nm, as shown in Figure 1c. The corresponding lattice fringes (Figure 1d) demonstrated highly-crystallized samples in agreement with the XRD results. The lattice spacing of 0.265 nm agreed well with the (131) spacing of orthorhombic Bi_2MoO_6. The effects of various synthesis conditions on the structure of Bi_2MoO_6 hollow spheres were examined in order to develop a comprehensive understanding of the formation mechanisms. Hence, only the main synthesis variables – polymer concentration and solvothermal temperature – were adjusted. It was found that the copolymer concentration has a direct effect on the formation of hollow Bi_2MoO_6.

The XRD patterns of the samples synthesized under different copolymer concentrations are shown in Figure 2a and indicate a high-degree of atomic ordering in the polycrystalline spheres. SEM images demonstrate the resultant mesostructure is dependent on the surfactant concentration (Figure 2b-d). When the synthesis was conducted in the absence of P123 (the solid Bi_2MoO_6

sample), only crystals with irregular shapes were obtained. The sample with a relatively low P123 concentration of 1 g exhibited a solid sphere structure with no hollow structures. As the P123 concentration was increased to 2g, hollow Bi_2MoO_6 spheres with diameters on the order of 300–400 nm and shell thickness of ~60–80 nm were obtained. Increasing the P123 weight to 3g resulted in the formation of the hollow Bi_2MoO_6 spheres with relatively large diameters (1–1.5 μm) and a slight increase in shell thickness (~100 nm). P123 includes hydrophilic polyoxyethylene (PEO) blocks on each side of a liner hydrophobic polyoxypropylene (PPO) block with a moderate molecular weight (M_{avg} = 5800). We purpose that as the concentration of P123 exceeds the critical micelle concentration in water-buthanol polar solutions, the conditions favors the formation of inverse micelles with dehydrated PPO blocks in the cores and hydrated PEO portions in the coronas.[25-27] The reaction conditions favors arrangement and then coalescence of the inverse micelles into micellar vesicle aggregations.[5, 28-30] It is likely that the outer surfaces of these formed P123 vesicles interact with the metal precursors through hydrogen bonding resulting in nanoparticle aggregation to form the hollow spherical shells.[5] The core portion consisting of polymer and anhydrous solvent is removed after calcination leaving a vacant region inside the shell made of inorganic materials (as depicted in Scheme 1). The formation process is complicated and governed by parameters such as the polymer concentration, temperature, and pH value. For instance, we observed that at pH values of 5, 7 and 9 no hollow structures were obtained (See Figure S2, Supporting Information) as opposed to the pH we have used in hollow structure formation (pH = 3).

In order to reveal the role of the solvothermal temperature on the formation of hollow Bi_2MoO_6 spheres, the autoclave process was carried out at 120, 140, 160 and 180 °C for 3 h (see Figure S3, Supporting Information). When the temperature was held at 160 °C, well dispersed hollow sphere were obtained as shown in Figure 1b. The sample prepared at 120 °C included hierarchically structured solids which were formed by self-assembly of nanosheets, and hollow microspheres were not observed. Hollow microspheres were also obtained at 140 and 180 °C, but the morphologies were not as homogenous as at 160 °C. This can be due to a change in the adsorption ability of the metal precursors to the vesicle surface altering the final morphology of the nanoparticles.[31]

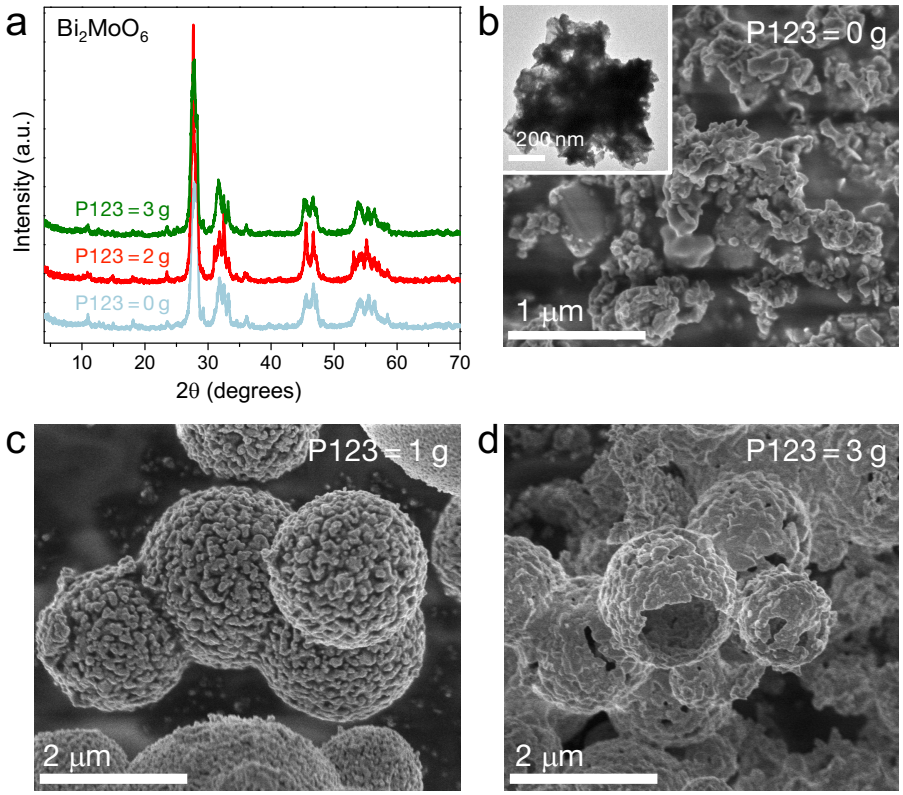

Figure 2. *(a) XRD patterns of Bi_2MoO_6 samples synthesized using different copolymer concentrations. SEM images of Bi_2MoO_6 obtained at 160 °C for 3 h using a solvothermal reaction method (b) without P123 [solid Bi_2MoO_6, (b,inset) corresponding TEM image], (c) with 1g P123, and (d) with 3 g P123.*

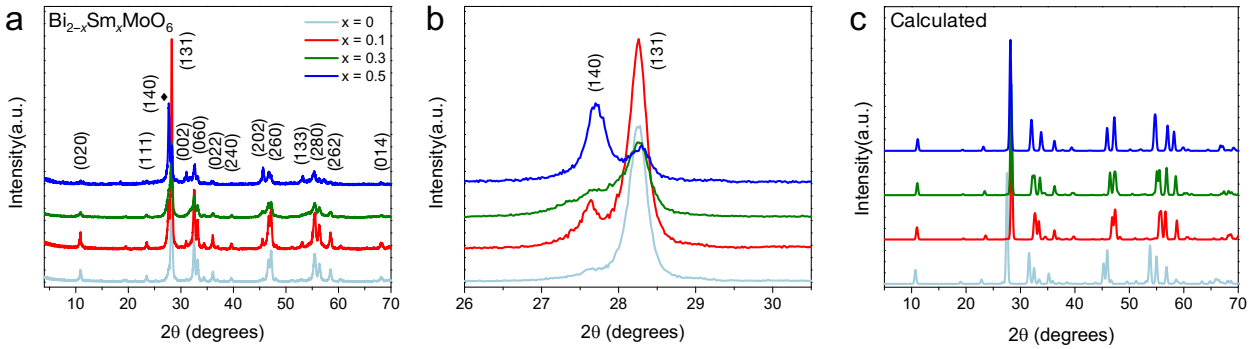

Figure 3. *(a) XRD pattern of the $Bi_{2-x}Sm_xMoO_6$ ($0 \leq x \leq 0.5$) and the corresponding magnified region in the vicinity of (140) and (131) peaks. (c) Simulated XRD pattern of $Bi_{2-x}Sm_xMoO_6$ at different concentrations.*

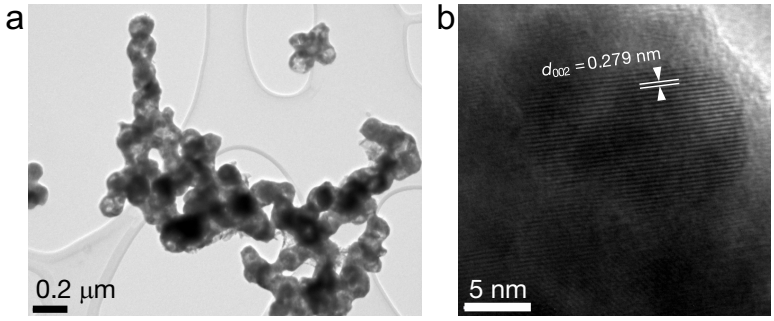

Figure 4. *(a) Low- and (b) high- resolution TEM images of* $Bi_{1.5}Sm_{0.5}MoO_6$.

Effect of Sm-doping on structure and morphology of $Bi_{2-x}Sm_xMoO_6$. XRD patterns of $Bi_{2-x}Sm_xMoO_6$ (x = 0, 0.1, 0.3 and 0.5) are shown in Figure 3a,b. The results can be indexed to the orthorhombic phase of Bi_2MoO_6 with no diffraction peaks associated with Sm_2O_3, suggesting the formation of a single phase bismuth samarium molybdate solid solution. The XRD peaks shift slightly toward the higher angles with increasing x owing to the lattice parameter changes resulting from the smaller ionic radius of Sm^{3+} (0.958Å) compared to Bi^{3+} (1.03 Å).[32] The DFT-calculated XRD patterns shown in Figure 3c were in agreement with the experimental results and the calculated Sm-doped structure (Scheme 1b). Crystallite size calculations were performed using the (131) reflection based on the Scherrer broadening method (Table 1) indicate a reduction in the crystallite size after Sm doping, which was confirmed by TEM (Figure 4). It can be seen that the hollow structure was preserved and the average sphere diameters approached 120–160 nm along with a shell thickness of around 10–30 nm. The corresponding lattice fringes shown in the HRTEM image are indicative of the local crystallinity. The lattice d-spacing of 0.279 nm corresponded to the (002) plane of the orthorhombic phase within 1.5%. The particle sizes of $Bi_{1.9}Sm_{0.1}MoO_6$ and $Bi_{1.7}Sm_{0.3}MoO_6$ were estimated as 50–100 nm and 75–120 nm shown in the TEM images in Figure S4a,b in the Supporting Information, respectively.

Table 1. *The measured and DFT-calculated band gaps and lattice parameters of the hollow microspherical $Bi_{2-x}Sm_xMoO_6$ samples.*

Summary of band gap energies			Lattice parameters						
Sample	Measured optical band gap energy [a] (eV)	Calculated band gap energy (eV)	Calculated			Measured [b]			
			a (Å)	*b* (Å)	*c* (Å)	*a* (Å)	*b* (Å)	*c* (Å)	Crystallite size (nm)
Bi_2MoO_6	2.74 ± 0.054	2.25	5.60	16.60	5.63	5.51 ± 0.04	16.21 ± 0.13	5.50 ± 0.00	32.8 ± 1.1
$Bi_{1.9}Sm_{0.1}MoO_6$	2.61 ± 0.031	1.89	5.50	16.67	5.62	5.48 ± 0.01	16.2 ± 0.04	5.51 ± 0.00	27.9 ± 1.3
$Bi_{1.7}Sm_{0.3}MoO_6$	2.69 ± 0.042	1.94	5.55	15.99	5.48	5.48 ± 0.00	16.25 ± 0.00	5.51 ± 0.00	24.4 ± 2.9
$Bi_{1.5}Sm_{0.5}MoO_6$	2.76 ± 0.077	2.02	5.58	15.92	5.53	5.51 ± 0.00	16.16 ± 0.01	5.48 ± 0.00	18.1 ± 1.1

[a] Uncertainty analysis: mean optical band gap and uncertainty were determined using the *x*-intercept of a linear curve fitted to the linear section of the absorbance data.

[b] Uncertainty analysis: mean crystallite size is obtained by Scherrer analysis of the FWHM of the following peaks: [020], [131], [002], [260], and [133]; mean lattice parameters were obtained using Bragg's law for the orthorhombic phase from the following peaks: [020], [111], [131], [002], and [060]. Uncertainty for both unit cell parameters and crystallite size was defined as one standard deviation above/below the mean.

XPS analysis was performed to study the bonding nature of the Sm ions as shown in Figure 5 for the $x = 0.3$ sample, and indicates substitutional doping of Sm on Bi atomic sites. The binding energy of Bi^{3+} $4f_{7/2}$ in $Bi_{1.7}Sm_{0.3}MoO_6$ was ~159.35 eV, which was slightly higher than that of un-doped Bii_2MoO_6 (158.79 eV, see Figure S5b, Supporting Information), but within the range of equipment uncertainty (~0.4 eV). The Sm $3d_{5/2}$ peak centered at 1086.09 eV is far from the binding energy reported for samarium oxide, 1083–1084 eV.[33-36] The O 1s core level spectrum (Figure 5d) was deconvoluted into four peaks. The small peak at 534.3 eV was related to the OH groups on the surface of the material. The main peak at 531.5 eV can be attributed to the oxygen in Sm─O groups.[34] The binding energy of O 1s decreases from 529.03 eV to 528.99 eV which may be due to the Sm-doping, but again this is within instrument uncertainty. The obtained XPS results also suggested the possible formation of the Bi─O─Sm bonds in the $Bi_{2-x}Sm_xMoO_6$ samples. The XPS survey and high resolution spectra of the un-doped Bi_2MoO_6 sample are shown in Figure S5 in the Supporting Information.

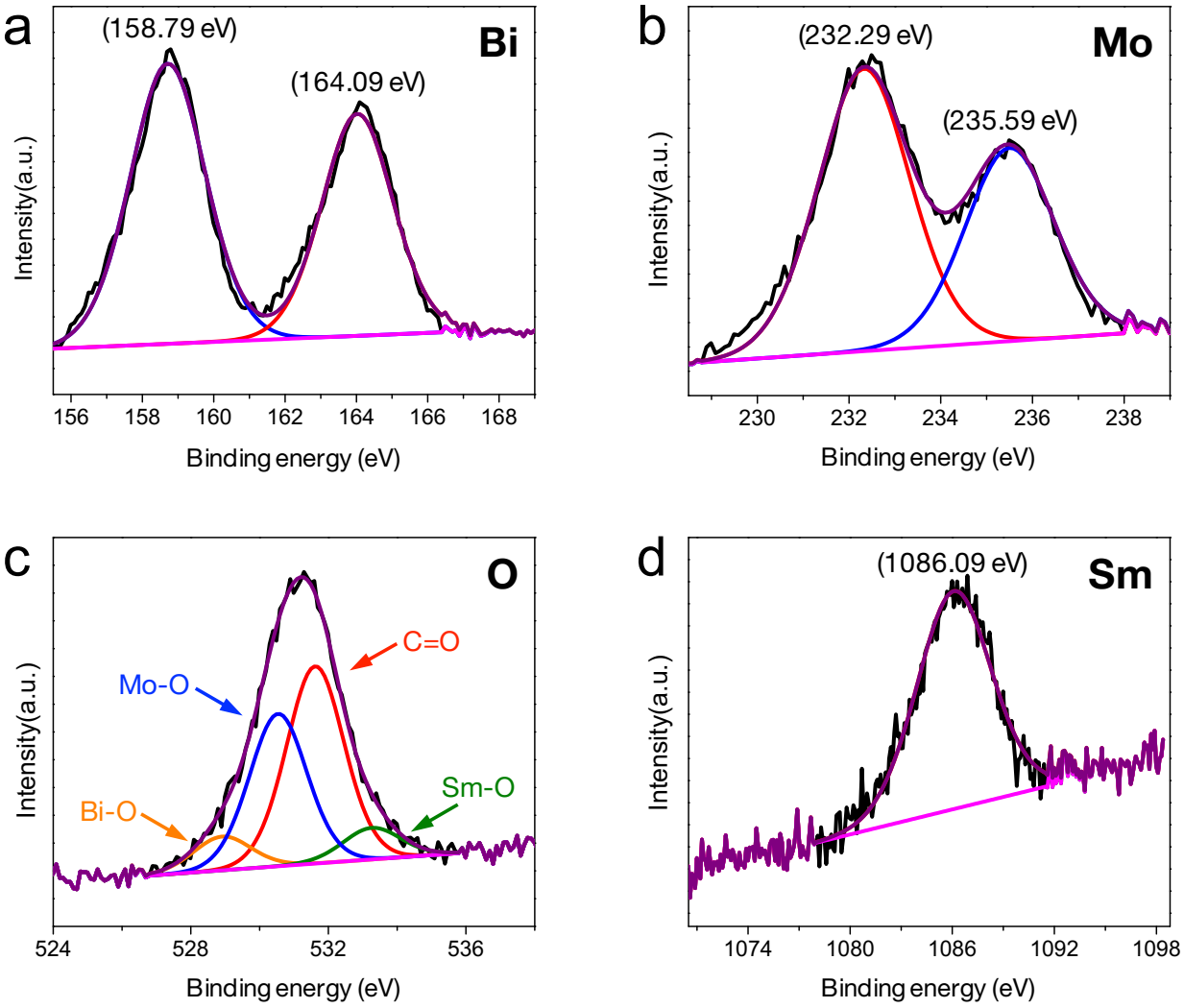

Figure 5. *XPS spectra of $Bi_{1.7}Sm_{0.3}MoO_6$ for the (a) Mo 3d, (b) Bi 4f, (c) Sm 3d, and (d) O 1s peaks.*

Chemical concentrations of Bi, Sm and Mo measured by ICP-OES are presented in Table 2 for each sample. The ICP-OES results indicate that the Sm concentrations were 19.8, 0.07 and 0.0% lower than those of the intended stoichiometric values calculated from the amount of the used precursors for $x = 0.1$, 0.3 and 0.5 samples, respectively. Furthermore, STEM/EDS analysis of the $x = 0.3$ sample showed a uniform concentration of each element in the material (Figure 6).

Table 2. *Measured BET surface area, precursor and measured ICP-OES concentrations of Bi, Sm and Mo for the hollow microspherical* $Bi_{2-x}Sm_xMoO_6$ *samples.*

Sample	BET surface area ($m^2\ g^{-1}$)	Precursor concentration (at.%)			Measured ICP-OES (at.%)		
		Bi	*Sm*	*Mo*	*Bi*	*Sm*	*Mo*
Bi_2MoO_6	5.46	66.67	--	33.34	75.63	--	24.37
$Bi_{1.9}Sm_{0.1}MoO_6$	7.09	63.35	3.30	33.34	68.76	2.65	28.59
$Bi_{1.7}Sm_{0.3}MoO_6$	23.59	56.67	10	33.34	61.89	9.32	28.79
$Bi_{1.5}Sm_{0.5}MoO_6$	29.60	50	16.67	33.34	60.66	16.77	22.56

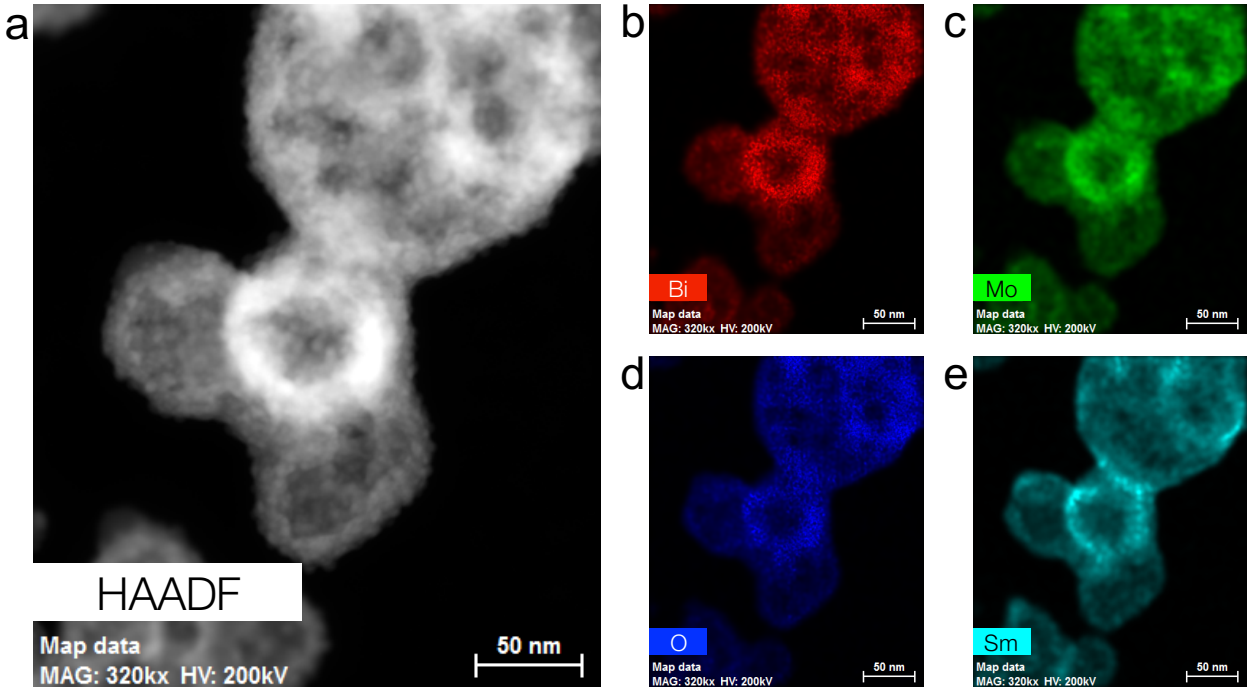

Figure 6. *STEM/EDS chemical map of* $Bi_{1.7}Sm_{0.3}MoO_6$*. (a) HAADF, (b) Bi (L-edge), (c) Mo (L-edge), (d) Sm (L-edge) and (e) O (K-edge).*

The Raman spectra of $Bi_{2-x}Sm_xMoO_6$ (x = 0, 0.1, 0.3 and 0.5) are shown in Figure 7. For Bi_2MoO_6 which consists of $(MoO_4)^{2-}$ with perovskite-like and $(Bi_2O_2)^{2+}$ with fluorite-like layers, six Raman active modes of vibrations were detected in the range of 100–850 cm^{-1}. The vibration peak at 146 cm^{-1} was related to the lattice mode of Bi^{3+} atoms. The Raman modes near 287 cm^{-1} were attributed to the E_g bending vibrations while the peaks at 356 and 408 cm^{-1} corresponded to the E_u symmetric bending. The mode at 717 cm^{-1} was from the asymmetric stretching vibration

mode of the MoO_6 octahedra. The A_{1g} mode at 802 cm^{-1} and A_{2u} mode at 852 cm^{-1} were attributed to the symmetric and asymmetric stretching vibrations of the Mo—O bonds in MoO_6 octahedra.[37, 38] As compared with the pure Bi_2MoO_6, the Raman spectra of Sm-doped samples have several different features. The most intense band for pure Bi_2MoO_6 appears at about 803 cm^{-1} where corresponded to the A_{1g} mode. In the case of $Bi_{2-x}Sm_xMoO_6$, as the samarium concentration increases this mode shifts slightly towards higher wave numbers. This shift can be attributed to the substitution of Bi ions with Sm ions, and the absence of peaks associated with Sm_2O_3 (344 cm^{-1} for cubic Sm_2O_3 [39]), in agreement with the observations from the XRD and XPS data. Furthermore, by increasing the Sm concentration, the Raman peaks became broader and weaker.

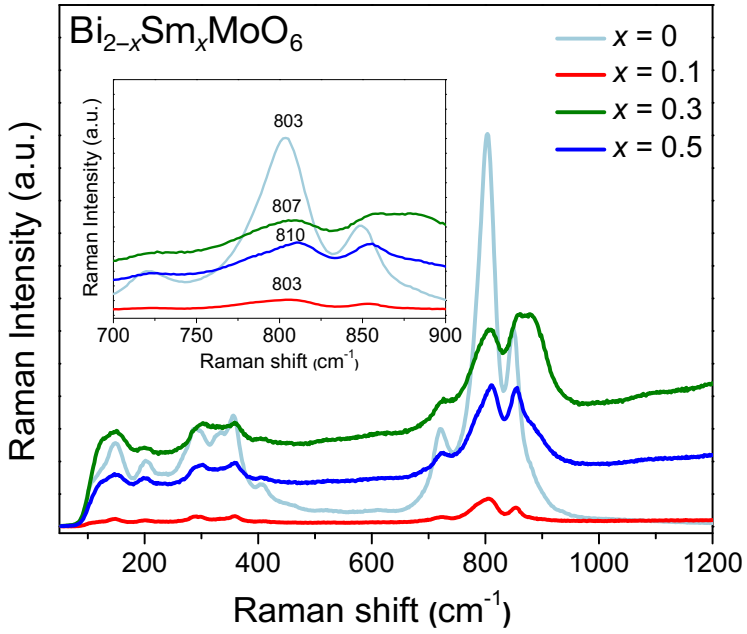

Figure 7. *Raman spectra of the $Bi_{2-x}Sm_xMoO_6$ samples for x = 0, 0.1, 0.3 and 0.5. The inset shows the region between 700 and 900 cm^{-1}.*

In addition, the optical absorption properties of all samples were studied using UV-Vis diffuse reflectance spectroscopy. The absorption ranges of the pure (x = 0) and the doped (x = 0.1, 0.3, and 0.5) samples ranges from 200 to ~440 nm in agreement with the yellowish color of the samples (Figure S7, Supporting Information). Weak light absorption was observed for the undoped solid Bi_2MoO_6 sample whereas improved absorption behaviors were detected for the hollow structured and Sm-doped cases. The sample with doping concentration of x = 0.3 exhibited the

strongest absorbance. By increasing the doping concentration further to x = 0.5 the absorbance intensity decreases by 16% which is still higher than those of x = 0.1 and pure samples. The estimated optical band gap energies (E_g) of the products were determined using the conversion ratio of $E_g = 1240/\lambda$ where λ is the wavelength of the absorption edge obtained by the intercept of a tangential line fitted on the absorption spectra with the wavelength axis. The measured optical and calculated band gaps are reported in Table 1.

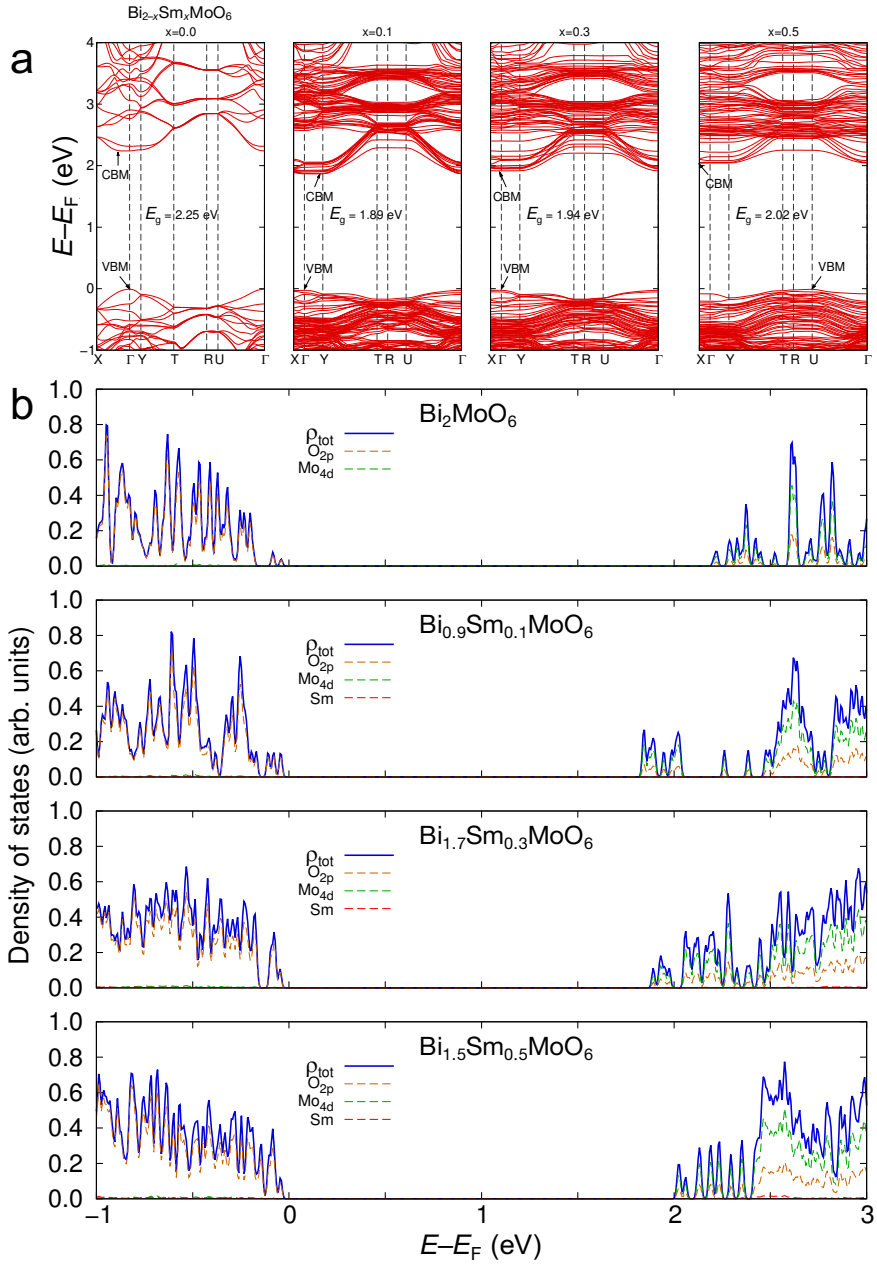

Figure 8. *(a) DFT-calculated electronic band structures and (b) corresponding total and orbital angular momentum projected DOS for pure Bi_2MoO_6 and $Bi_{2-x}Sm_xMoO_6$ (x = 0.1, 0.3 and 0.5).*

It was observed that the optical band gaps of $x = 0.1$, and 0.3 were 0.11 and 0.02 eV lower (slightly) than 2.77 eV for the pure Bi_2MoO_6 sample. However, the band gap of $x = 0.5$ was 0.04 eV higher than that of the pure Bi_2MoO_6 which can be due to experimental variations. The DFT-calculated band gaps showed a similar trend to that observed experimentally, the calculated band gap for $x = 0.5$ was higher than those for $x = 0.1$ and 0.3. The calculated electronic band structures of pure Bi_2MoO_6 and three doped models with $x = 0.1$, 0.3, and 0.5 are given in Figure 8a, showing that Bi_2MoO_6 is an indirect band gap semiconductor with the valence band maximum (VBM) residing at the Γ point while the conduction band minimum (CBM) is slightly deflected from the Γ point towards the X point. Because the lowest conduction band is very flat near the Γ point, Bi_2MoO_6 can be considered a quasi-direct band gap material. This conclusion is essentially applicable for low-doping concentrations ($x = 0.1$ and 0.3) while for $x = 0.5$, the CBM shifts to the U point, making highly alloyed $Bi_{2-x}Sm_xMoO_6$ a classic indirect band gap material. Overall, the band gap reduction by Sm doping is very small. We then attempted to clarify the roles of the dopants by showing in Figure 8b the electronic densities of states (DOS) of pure and doped models. In pure Bi_2MoO_6, the VBM was dominated by the O 2p states while major contributions to the CBM come from the Mo 4d states and, at a lower level, the O 2p states. Contributions from Bi-originated states were negligible. Presumably, this was why the contributions of Sm dopants to the states near the VBM and CBM of the doped models are also very small. Therefore, the small band gap reduction in $Bi_{2-x}Sm_xMoO_6$ was a consequence of the small lattice deformation rather than a direct contribution from the dopants. At high Sm concentrations ($x = 0.3$ and 0.5), the lattice deformations may be partly cancelled out, leading to the largest band gap reduction at $x = 0.1$ as revealed in Table 1 and Figure 8.

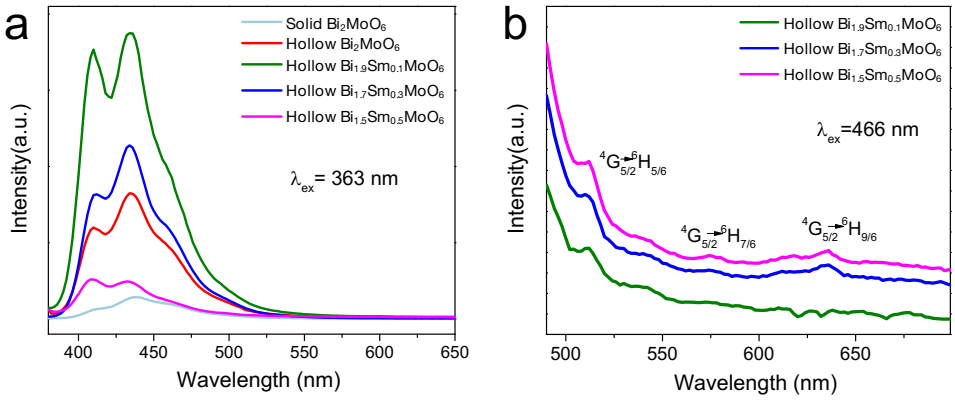

Figure 9. *Emission spectra of $Bi_{2-x}Sm_xMoO_6$ with different Sm concentrations (x = 0, 0.1, 0.3 and 0.5) excited at λ_{ex} = (a) 363 nm and (b) 466 nm.*

Photoluminescence (PL) properties. The room-temperature photoluminescence spectra of solid and hollow spherical $Bi_{2-x}Sm_xMoO_6$ is shown in Figure 9 using excitation lines of 363 and 466 nm. All of the samples exhibited emissions centered around 436 nm (2.8 eV) followed by shoulder peaks at ~410 nm (3.0 eV). At 466 nm excitation, characteristic emission peaks at 564, 601, 611, 647 were assigned to $^6H_{5/2}$, $^6H_{7/2}$, $^6H_{9/2}$, and $^6H_{11/2}$ Sm transitions, respectively.[40] A comparison between the hollow and solid structured samples indicates an enhancement ratio of 5.79 in the peak intensity at 436 nm, likely due to multiple reflections and scattering in the hollow structures.[1] The emission intensities are enhanced at lower Sm content (x = 0.1 and 0.3), and further increase in Sm concentration (x = 0.5) resulted in a sharp decrease in the emission intensity. The x = 0.1 sample exhibited the highest intensity, 2.28 times higher than that of the undoped hollow structured Bi_2MoO_6 and 13.2 times higher than the solid Bi_2MoO_6. Based on our DFT calculations, this enhancement for the doped samples likely results from a large number of electronic states introduced near the CBM of $Bi_{1.9}Sm_{0.1}MoO_6$. The complete emission-excitation spectra of hollow Bi_2MoO_6 spheres showed that maximum emissions were obtained under excitation from 360 to 390 nm (Figure S8, Supporting Information). Another factor that should be mentioned is the effect of the surface area on the PL properties of the materials. It has been observed that the PL intensity decreases with increasing surface area[41] although these effects were found to be small compared to the other parameters.[42] This trend is in agreement with the BET surface area of the Sm-doped samples reported in Table 2 and the related N_2 adsorption isotherms (Figure S9, Supporting Information). The relative PL intensities for samples with different mean particle sizes are shown in Figure S10 of the Supporting Information and indicate a lack of correlation between size and

peak intensity in our samples. We note it is likely that resonant effects will occur at optimal sizes in these materials further increasing peak emission intensity, and should be addressed in future work through thorough parametric analysis.

Summary and Conclusions

A solvothermal synthesis method involving soft templation by P123 has been demonstrated for the production of hollow spherical structures of $Bi_{2-x}Sm_xMoO_6$ with $0 \leq x \leq 0.5$. The optical and photoluminescence properties of the hollow structured samples compared to the solid sample shows remarkable enhancement, with an order of magnitude improvement in the fluorescence intensity for hollow $Bi_{1.9}Sm_{0.1}MoO_6$ microspheres compared to solid Bi_2MoO_6. An experimental procedure supported by DFT calculations was used to study the changes in the electronic structure due to the doping, and indicate transition from a quasi-direct electronic band gap at low Sm concentration to an indirect band gap at high Sm concentration is responsible for fluorescence quenching in the $x = 0.5$ sample. The results of the present investigation have potential applications in the modifications of bismuth molybdate-based materials.

Acknowledgement. This work was partially supported by the National Science Foundation under Grant No. CAREER-1553987 (M.T.P., S.Y.), the UConn Research Foundation, award number PD15-0067 (S.Y., R.K.-S.), and a GE Graduate Fellowship for Innovation (S.Y.). TEM studies were conducted using facilities in the UConn/FEI Center for Advanced Microscopy and Materials Analysis (CAMMA).

Supporting information available. TGA analysis of Bi_2MoO_6 samples before calcination, FTIR spectra of hollow Bi_2MoO_6 after removing P123, XRD patterns and SEM images of Bi_2MoO_6 samples obtained after removing P123 at different calcination temperatures, survey and high resolution XPS of hollow Bi_2MoO_6, UV-Vis absorption spectra of hollow $Bi_{2-x}Sm_xMoO_6$, and emission-excitation map of hollow Bi_2MoO_6 microspheres.

References

(1) Chen, M., Ye, C., Zhou, S., and Wu, L. Recent advances in applications and performance of inorganic hollow spheres in devices, *Adv. Mater.* **2013**, *25*, 5343-5351. http://dx.doi.org/10.1002/adma.201301911

(2) Hu, J., Chen, M., Fang, X., and Wu, L. Fabrication and application of inorganic hollow spheres, *Chem. Soc. Rev.* **2011**, *40*, 5472-5491. http://dx.doi.org/10.1039/C1CS15103G

(3) Lai, X., Halpert, J. E., and Wang, D. Recent advances in micro-/nano-structured hollow spheres for energy applications: From simple to complex systems, *Energy Environ. Sci.* **2012**, *5*, 5604-5618. http://dx.doi.org/10.1039/C1EE02426D

(4) Ye, T., Dong, Z., Zhao, Y., Yu, J., Wang, F., Zhang, L., and Zou, Y. Rationally fabricating hollow particles of complex oxides by a templateless hydrothermal route: the case of single-crystalline $SrHfO_3$ hollow cuboidal nanoshells, *Dalton Trans.* **2011**, *40*, 2601-2606. http://dx.doi.org/10.1039/C0DT01354D

(5) Wang, X., Feng, J., Bai, Y., Zhang, Q., and Yin, Y. Synthesis, properties, and applications of hollow micro-/nanostructures, *Chem. Rev.* **2016**, 10983−11060. http://dx.doi.org/10.1021/acs.chemrev.5b00731

(6) Qi, J., Lai, X., Wang, J., Tang, H., Ren, H., Yang, Y., Jin, Q., Zhang, L., Yu, R., Ma, G., Su, Z., Zhao, H., and Wang, D. Multi-shelled hollow micro-/nanostructures, *Chem. Soc. Rev.* **2015**, *44*, 6749-6773. http://dx.doi.org/10.1039/C5CS00344J

(7) Zhang, Q., Wang, W., Goebl, J., and Yin, Y. Self-templated synthesis of hollow nanostructures, *Nano Today* **2009**, *4*, 494-507. http://dx.doi.org/10.1016/j.nantod.2009.10.008

(8) Shimodaira, Y., Kato, H., Kobayashi, H., and Kudo, A. Photophysical properties and photocatalytic activities of bismuth molybdates under visible light irradiation, *J. Phys. Chem. B* **2006**, *110*, 17790-17797. http://dx.doi.org/10.1021/jp0622482

(9) Frit, B. and Mercurio, J. P. The crystal chemistry and dielectric properties of the Aurivillius family of complex bismuth oxides with perovskite-like layered structures, *J. Alloys Compd.* **1992**, *188*, 27-35. http://dx.doi.org/10.1016/0925-8388(92)90639-Q

(10) Ma, Y., Jia, Y., Jiao, Z., Yang, M., Qi, Y., and Bi, Y. Hierarchical Bi_2MoO_6 nanosheet-built frameworks with excellent photocatalytic properties, *Chem. Commun.* **2015**, *51*, 6655-6658. http://dx.doi.org/10.1039/C5CC00634A

(11) Sim, L. T., Lee, C. K., and West, A. R. High oxide ion conductivity in Bi_2MoO_6 oxidation catalyst, *J. Mater. Chem.* **2002**, *12*, 17-19. http://dx.doi.org/10.1039/B106792N

(12) Dai, Z., Qin, F., Zhao, H., Tian, F., Liu, Y., and Chen, R. Time-dependent evolution of the $Bi_{3.64}Mo_{0.36}O_{6.55}/Bi_2MoO_6$ heterostructure for enhanced photocatalytic activity via the interfacial hole migration, *Nanoscale* **2015**, *7*, 11991-11999. http://dx.doi.org/10.1039/C5NR02745D

(13) Zhang, X. B., Zhang, L., Hu, J. S., and Huang, X. H. Facile hydrothermal synthesis and improved photocatalytic activities of Zn^{2+} doped Bi_2MoO_6 nanosheets, *RSC Adv.* **2016**, *6*, 32349-32357. http://dx.doi.org/10.1039/c6ra06972j

(14) Shang, M., Wang, W., Ren, J., Sun, S., and Zhang, L. Nanoscale Kirkendall effect for the synthesis of Bi_2MoO_6 boxes via a facile solution-phase method, *Nanoscale* **2011**, *3*, 1474-1476. http://dx.doi.org/10.1039/C0NR00974A

(15) Tian, G., Chen, Y., Zhou, W., Pan, K., Dong, Y., Tian, C., and Fu, H. Facile solvothermal synthesis of hierarchical flower-like Bi_2MoO_6 hollow spheres as high performance visible-light driven photocatalysts, *J. Mater. Chem.* **2011**, *21*, 887-892. http://dx.doi.org/10.1039/C0JM03040F

(16) Zhang, M., Shao, C., Mu, J., Huang, X., Zhang, Z., Guo, Z., Zhang, P., and Liu, Y. Hierarchical heterostructures of Bi_2MoO_6 on carbon nanofibers: Controllable solvothermal fabrication and enhanced visible photocatalytic properties, *J. Mater. Chem.* **2012**, *22*, 577-584. http://dx.doi.org/10.1039/C1JM13470A

(17) Yin, W., Wang, W., and Sun, S. Photocatalytic degradation of phenol over cage-like Bi_2MoO_6 hollow spheres under visible-light irradiation, *Catal. Commun.* **2010**, *11*, 647-650. http://dx.doi.org/10.1016/j.catcom.2010.01.014

(18) Zhang, J., Liu, Y., Li, L., Zhang, N., Zou, L., and Gan, S. Hydrothermal synthesis, characterization, and color-tunable luminescence properties of Bi_2MoO_6:Eu^{3+} phosphors, *RSC Adv.* **2015**, *5*, 29346-29352. http://dx.doi.org/10.1039/C5RA03913D

(19) Alemi, A. A., Kashfi, R., and Shabani, B. Preparation and characterization of novel Ln (Gd^{3+}, Ho^{3+} and Yb^{3+})-doped Bi_2MoO_6 with Aurivillius layered structures and photocatalytic activities under visible light irradiation, *J. Mol. Catal. A: Chem.* **2014**, *392*, 290-298. http://dx.doi.org/10.1016/j.molcata.2014.05.029

(20) Han, B., Zhang, J., Li, P., Li, J., Bian, Y., and Shi, H. Synthesis and luminescence properties of Eu^{3+} doped high temperature form of Bi_2MoO_6, *J. Electron. Mater.* **2015**, *44*, 1028-1033. http://dx.doi.org/10.1007/s11664-014-3621-4

(21) Kresse, G. and Furthmüller, J. Efficiency of ab-initio total energy calculations for metals and semiconductors using a plane-wave basis set, *Comput. Mater. Sci.* **1996**, *6*, 15-50. http://dx.doi.org/10.1016/0927-0256(96)00008-0

(22) Kresse, G. and Furthmüller, J. Efficient iterative schemes for *ab initio* total-energy calculations using a plane-wave basis set, *Phys. Rev. B* **1996**, *54*, 11169-11186. http://dx.doi.org/10.1103/PhysRevB.54.11169

(23) Perdew, J. P., Burke, K., and Ernzerhof, M. Generalized gradient approximation made simple, *Phys. Rev. Lett.* **1996**, *77*, 3865-3868. http://dx.doi.org/10.1103/PhysRevLett.77.3865

(24) Monkhorst, H. J. and Pack, J. D. Special points for Brillouin-zone integrations, *Phys. Rev. B* **1976**, *13*, 5188-5192. http://dx.doi.org/10.1103/PhysRevB.13.5188

(25) Hunter, R. J. Foundations of Colloid Science. Oxford University Press: New York, **1987**. https://global.oup.com/academic/product/foundations-of-colloid-science-9780198505020

(26) Paschalis, A. and Hatton, T. A. Poly(ethylene oxide)-poly(propylene oxide)-poly(ethylene oxide) block copolymer surfactants in aqueous solutions and at interfaces: Thermodynamics, structure, dynamics, and modeling, *Colloids Surf., A* **1995**, *96*, 1-46. http://dx.doi.org/10.1016/0927-7757(94)03028-X

(27) Geng, J., Zhu, J.-J., Lu, D.-J., and Chen, H.-Y. Hollow $PbWO_4$ nanospindles via a facile sonochemical route, *Inorg. Chem.* **2006**, *45*, 8403-8407. http://dx.doi.org/10.1021/ic0608804

(28) Geng, J., Zhu, J.-J., Lu, D.-J., and Chen, H.-Y. Hollow $PbWO_4$ nanospindles via a facile sonochemical route, *Inorg. Chem.* **2006**, *45*, 8403−8407. http://dx.doi.org/10.1021/ic0608804

(29) Wei, H., Yu, C.-y., Chang, C., Quan, C.-y., Mo, S.-b., Cheng, S.-x., Zhang, X.-z., and Zhuo, R.-x. Direct observation of time and temperature dependent transition from spherical micelles to vesicles, *Chem. Commun.* **2008**, 4598−4600. http://dx.doi.org/10.1039/B811553B

(30) Zheng, X., Xie, Y., Zhu, L., Jiang, X., and Yan, A. Formation of vesicle-templated CdSe hollow spheres in an ultrasound-induced anionic surfactant solution, *Ultrason. Sonochem.* **2002**, *9*, 311−316. http://dx.doi.org/10.1016/S1350-4177(02)00086-X

(31) Li, S.-K., Li, C.-H., Huang, F.-Z., Wang, Y., Shen, Y.-H., Xie, A.-J., and Wu, Q. One-pot synthesis of uniform hollow cuprous oxide spheres fabricated by single-crystalline particles via a simple solvothermal route, *J. Nanopart. Res.* **2011**, *13*, 2865−2874. http://dx.doi.org/10.1007/s11051-010-0175-0

(32) Shannon, R. D. Revised effective ionic radii and systematic studies of interatomic distances in halides and chalcogenides, *Acta Crystallogr., Sect. A* **1976**, *32*, 751-767. http://dx.doi.org/10.1107/S0567739476001551

(33) Mason, M. G., Lee, S. T., Apai, G., Davis, R. F., Shirley, D. A., Franciosi, A., and Weaver, J. H. Particle-size-induced valence changes in samarium clusters, *Phys. Rev. Lett.* **1981**, *47*, 730-733. http://dx.doi.org/10.1103/PhysRevLett.47.730

(34) Nguyen, T.-D., Mrabet, D., and Do, T.-O. Controlled self-assembly of Sm_2O_3 nanoparticles into nanorods: Simple and large scale synthesis using bulk Sm_2O_3 powders, *J. Phys. Chem. C* **2008**, *112*, 15226-15235. http://dx.doi.org/10.1021/jp804030m

(35) Nguyen, T.-D., Dinh, C.-T., and Do, T.-O. Monodisperse samarium and cerium orthovanadate nanocrystals and metal oxidation states on the nanocrystal surface, *Langmuir* **2009**, *25*, 11142-11148. http://dx.doi.org/10.1021/la901387q

(36) Hodgson, G. K., Impellizzeri, S., Hallett-Tapley, G. L., and Scaiano, J. C. Photochemical synthesis and characterization of novel samarium oxide nanoparticles: Toward a heterogeneous Bronsted acid catalyst, *RSC Adv.* **2015**, *5*, 3728-3732. http://dx.doi.org/10.1039/C4RA14841J

(37) Hardcastle, F. D. and Wachs, I. E. Molecular structure of molybdenum oxide in bismuth molybdates by Raman spectroscopy, *J. Phys. Chem.* **1991**, *95*, 10763-10772. http://dx.doi.org/10.1021/j100179a045

(38) Kongmark, C., Martis, V., Rubbens, A., Pirovano, C., Lofberg, A., Sankar, G., Bordes-Richard, E., Vannier, R.-N., and Van Beek, W. Elucidating the genesis of Bi_2MoO_6 catalyst by combination of synchrotron radiation experiments and Raman scattering, *Chem. Commun.* **2009**, 4850-4852. http://dx.doi.org/10.1039/B907935A

(39) Dilawar, N., Mehrotra, S., Varandani, D., Kumaraswamy, B. V., Haldar, S. K., and Bandyopadhyay, A. K. A Raman spectroscopic study of C-type rare earth sesquioxides, *Mater. Charact.* **2008**, *59*, 462-467. http://dx.doi.org/10.1016/j.matchar.2007.04.008

(40) Duan, T.-W. and Yan, B. Lanthanide ions (Eu^{3+}, Tb^{3+}, Sm^{3+}, Dy^{3+}) activated ZnO embedded zinc 2,5-pyridinedicarboxylic metal-organic frameworks for luminescence application, *J. Mater. Chem. C* **2015**, *3*, 2823-2830. http://dx.doi.org/10.1039/C4TC02893G

(41) Wang, W.-N., Widiyastuti, W., Ogi, T., Lenggoro, I. W., and Okuyama, K. Correlations between crystallite/particle size and photoluminescence properties of submicrometer phosphors, *Chem. Mater.* **2007**, *19*, 1723−1730. http://dx.doi.org/10.1021/cm062887p

(42) Jung, K. Y., Lee, C. H., and Kang, Y. C. Effect of surface area and crystallite size on luminescent intensity of Y_2O_3:Eu phosphor prepared by spray pyrolysis, *Mater. Lett.* **2005**, *59*, 2451−2456. http://dx.doi.org/10.1016/j.matlet.2005.03.017